IOP Conf. Series: Journal of Physics: Conf. Series **1312** (2019) 012008 doi:10.1088/1742-6596/1312/1/012008

The search for light dark matter with the NEWS-G spherical proportional counter

G. Giroux[1], P. Gros[2] and I. Katsioulas[3,4], on the behalf of the NEWS-G collaboration

[1] Arthur B. McDonald Canadian Astroparticle Physics Research Instititute, Department of Physics, Engineering Physics and Astronomy, Queen's University, Kingston, K7L 3N6, Canada
[2] Department of Physics, Engineering Physics and Astronomy, Queen's University, Kingston, K7L 3N6, Canada
[3] IRFU, CEA, Université Paris-Saclay, F-91191 Gif-Sur-Yvette, France
[4] School of Physics and Astronomy, University of Birmingham, B15 2TT, United Kingdom

E-mail: gg42@queensu.ca, pg72@queensu.ca, I.Katsioulas@bham.ac.uk

Abstract. The NEWS-G (New Experiment with Spheres - Gas) collaboration searches for dark matter in the form of low-mass Weakly Interacting Massive Particles (WIMPs) using Spherical Proportional Counters (SPCs) filled with gases with low atomic masses. The operation of SEDINE, a 60-cm diameter prototype SPC filled with a mixture of neon and methane and installed at the Laboratoire Souterrain de Modane (LSM) in France, recently set new constraints on the spin-independent WIMP-nucleon scattering cross-section in the sub-GeV/c^2 mass region. The collaboration is currently planning the installation a 140-cm ultra-low background SPC in a compact shielding at SNOLAB in Canada. Recent advances in radioactive background control, detector monitoring and sensor development, will provide for this next experimental phase of NEWS-G unprecedented sensitivity to low-mass WIMPs.

1. Introduction

A wealth of evidence supports the existence of non-baryonic cold dark matter in the universe [1, 2, 3]. Weakly interacting massive particles (WIMPs) [4] are a class of promising candidates that are emerging from beyond-the-Standard-Model theories. For example, supersymmetric extensions to the Standard Model give rise to a thermally produced WIMP with a mass typically ranging from 10 GeV/c^2 to 10 TeV/c^2 [5]. Direct detection experiments are relying on the expected coherent elastic scattering of the Milky Way halo WIMPs with detector target nuclei. These searches are notoriously challenging in part due to the small interaction cross-sections, leading to expected rates that are order of magnitudes smaller than the ones from natural radioactive backgrounds. Experiments using large liquid xenon time projection chambers (TPCs) are currently leading the direct search for SUSY WIMPs [22, 28], but the signal remains elusive. This, in addition to the lack of evidence for SUSY at LHC [6], warrants the extension of the search to low mass WIMPs. The exploration of low-mass, sub-GeV WIMPs, is further motivated by the predictions of several recent theoretical frameworks, such as dark sector [7, 8], asymmetric dark matter [9, 10], and generalized effective theory [11]. Direct detection experiments aiming at the detection of light WIMPs require extremely low thresholds to detect nuclear recoils with sub-keV energy, and light atomic mass targets to optimize momentum transfers.

2. The NEWS-G Spherical Proportional Counter

The NEWS-G collaboration aims at the search for light WIMPs using spherical proportional counters (SPCs) filled with light atomic mass gases [12, 13], such as neon, methane, and helium. The detector consists of a metallic spherical shell (shown in figure 1), held at ground potential. A small sensor is placed at the center of the sphere at the end of a grounded metallic rod, and is held at positive high voltage. The resulting electric field is mostly radial, except near the sensor rod which disturbs the field, and falls as $1/r^2$ (shown in figure 2). The interaction of a particle with the target gas creates the primary ionization, which is then drifted towards the center of the sphere along the electric field lines. As the electrons approach within approximately a mm the sensor, the magnitude of electric field becomes sufficient for the production of secondary ionization. The signal is generated by the ions drifting away from the sensor. The low capacitance of the sensor, which allows for low electronic noise, in combination with the large amplification of the signal, allows for single electron detection and therefore makes the SPC a powerful detector for low energy nuclear recoils.

Figure 1. Picture of SEDINE, a 60-cm diameter prototype SPC installed at the LSM in Modane.

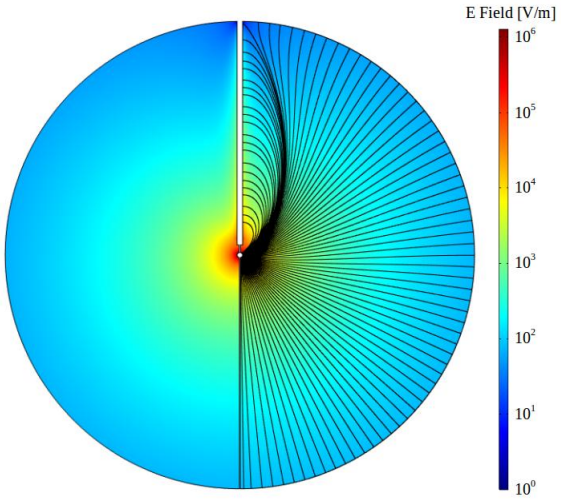

Figure 2. Cross-sectional view of the SPC with the rod and sensor visible in white. The electric-field-magnitude is shown in color, while the electric field lines are drawn on the right-side of the picture only.

3. Recent results from SEDINE

SEDINE is a 60-cm diameter SPC made from pure NOSV copper [14] and is installed at the Laboratoire Souterrain de Modane (LSM), in France, at a 4800 m water-equivalent depth, that is primarily a proof-of-concept for the use of large SPCs to search for low-mass dark matter. To mitigate the environmental radioactive backgrounds, the detector is placed inside a cubic shielding consisting of, from the inside to the outside, 8 cm of copper, 15 cm of lead, and 30 cm of high-density polyethylene. At the center of SEDINE, a grounded copper rod is holding a 6.3-mm silicon sensor held at high-voltage. The current induced on the sensor due to ions drifting away is shaped by a charge sensitive pre-amplifier, and is digitized at 2.08 MHz by the data acquisition system.

3.1. SEDINE dark matter search run

Between April and May 2015, while it was filled to a pressure of 3.1 bar with a mixture of 90.3% Neon and 0.7% CH_4, SEDINE ran in dark matter search mode uninterruptedly for 42.7 days. The details of pulse treatment, data analysis, and limit calculation were shown in details in [15].

3.2. Pulse treatment and backgrounds

For each events recorded by the data acquisition system, pulses are treated to extract the 2 main parameter if the analysis: the integrated charge, or energy, which is proportional to the total ionization collected by the sensor, and the pulse rise-time, which measure provides essential information on the location of the primary ionization. At energies below a few tens of keV, most of the background events are from radioactive decays of radon progeny at the inner surface of the copper sphere (e.g. β-decay of ^{210}Pb and auger electrons from de-excitation of ^{210}Bi*). These surface events typically have larger rise-time, due in part to primary ionization track length and to the longer drift time corresponding to a larger longitudinal and transverse diffusion. The background volume events are homogeneously distributed and consists mostly of electron-recoils from the natural contamination in gamma emitters from the laboratory environment, as well as from the construction materials of the shielding and detector.

3.3. Calibration and simulation

To understand the expected response of the detector to WIMPs, SEDINE was calibrated with an external Am-Be neutron source and an internal gaseous ^{37}Ar source. The *in-situ* calibration with ^{37}Ar allows for low-energy calibration with X-ray from electron capture in K-shell and L-shell at 2.82 keV and 270 eV respectively. The reconstructed energy of the 2.82 keV peak shows a dependence in rise-time which is attributed to electron attachment during drift, and the measurement of this dependence allows for a correction to this effect. A complete Monte-Carlo simulation of the events rise-time and energy was conducted and validated with experimental data. The simulation takes into account the transport of the primary ionization into the simulated electric field, the electron amplification near the sensor, and the signal generation through the data acquisition stream. Experimentally measured electronic noise is added to the pulses for a realistic production of simulated events. Finally, the simulated pulses undergo the

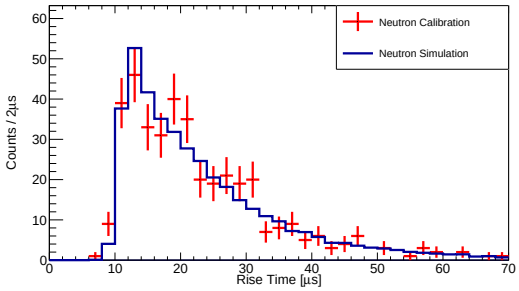

Figure 3. Rise-time distribution of volume events from a detector calibration with neutrons (red dots) compared with the Monte-Carlo simulation (blue histogram).

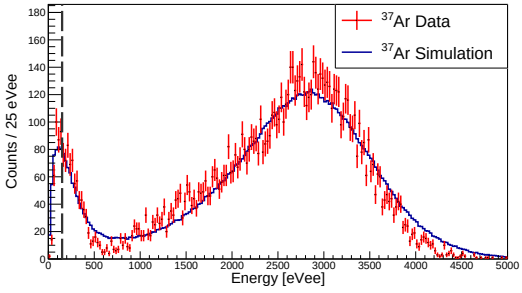

Figure 4. Energy spectrum of the detector calibration with an internal ^{37}Ar source (red dots) compared with the Monte-Carlo simulation. The two peaks from electron capture X-rays in the K-shell and L-shell at 2.82 keV and 270 eV respectively are clearly visible.

same pulse treatment and parameter evaluation than the real data. Figure 3 shows the excellent agreement between simulated and real rise-times from an Am-Be neutron calibration, for events between 150 eV_{ee} and 250 eV_{ee}, and figure 4 shows the agreement between the real and simulated energy spectra of an internal ^{37}Ar calibration.

3.4. Data analysis and results

The energy scale for the dark matter search data has been set by the 8 keV copper fluorescence peak that is present throughout the run. An analysis threshold of 150 eVee was chosen conservatively to ensure that there was 100% trigger efficiency for all events, especially events with long drift time that are affected by electron attachment to a greater extent. Pulse-shape based quality cuts were applied to remove non-physical events (micro-discharges). These cuts did not lead to a loss of signal efficiency other than dead time. A more significant loss of exposure (20.1%) comes from the 4 seconds dead time imposed after each event. This cut is applied to reject events that were identified as after-pulsing. To search for the WIMP signal, a preliminary region of interest (ROI) in the energy and rise-time space was set (rise-time [10, 32] μs, energy [150, 4000] eV_{ee}). The background in the ROI was estimated using data from the ROI's side bands, and extrapolated with the simulated data. The ROI was optimized for each WIMP masses using a Boosted Decision Tree (BDT) made from the energy and rise-time variables and trained on the simulated data. Figure 5 show the distribution in rise-time and energy of the 1620 events recorded during the physics run that are passing the quality cuts, as well as the events that pass the BDT cuts for 0.5 GeV/c^2 WIMPs and 16 GeV/c^2 WIMPs.

For each WIMP mass, the rate of events passing the BDT cut is converted into and upper limit at 90% confidence level on the WIMP-nucleon spin-independent scattering cross section. Figure 6 shows the exclusion limit as a function of the WIMP mass along the expected sensitivity region in the absence of a signal, calculated from toy-Monte-Carlo. These results set competitive constraints in the GeV/c^2 mass range, and at the time of publication, set the most stringent constraints for WIMPs below 0.6 GeV/c^2.

4. Status of NEWS-G at SNOLAB

The NEWS-G collaboration is planning the installation of a 140-cm diameter SPC made from ultra-pure copper (commercial C10100) (figure 7). This detector is the largest SPC to date and has been approved for installation at SNOLAB in Canada, at a 6000 m.w.e. depth. The SPC will be placed in a compact shielding as seen in figure 8. From the outside to the inside, the shield consists of 40 cm of borated polyethylene, and 22 cm of low activity lead (including the inner most 3 cm made from archaeological lead). The lead shield is placed into a stainless steel envelope that will be flushed with pure nitrogen to mitigate the presence of radon. A glove box system which allows for the replacement of the sensor and sensor rod without exposing the inside of the SPC to the radon-rich ambient air. All of the shielding and detector will be sitting on a seismic platform as a precaution for seismic events.

Monte-Carlo simulations of the detector shielding and detector construction material indicate that the leading source of background in the 140-cm SPC will be dominated by the natural content of ^{210}Pb in detector's copper. To mitigate this contamination, the hemispheric shells that were obtained from turning the copper disks have recently been electropolished and electroplated underground at LSM. A commissioning of the experiment is planned first at LSM during the summer 2019, while the polyethylene shielding is being fabricated in Canada. The construction of a neutron shielding based on a concentric cylindrical water tank at LSM will allow for a first short dark matter search run, before the detector is shipped to SNOLAB during Fall 2019. It is expected that the dark matter search at SNOLAB will begin in Winter 2020. Based on the strict control of the construction material radioactive background, as well as improvements in sensor performance, analysis methods, and detector monitoring, it is expected that this dark

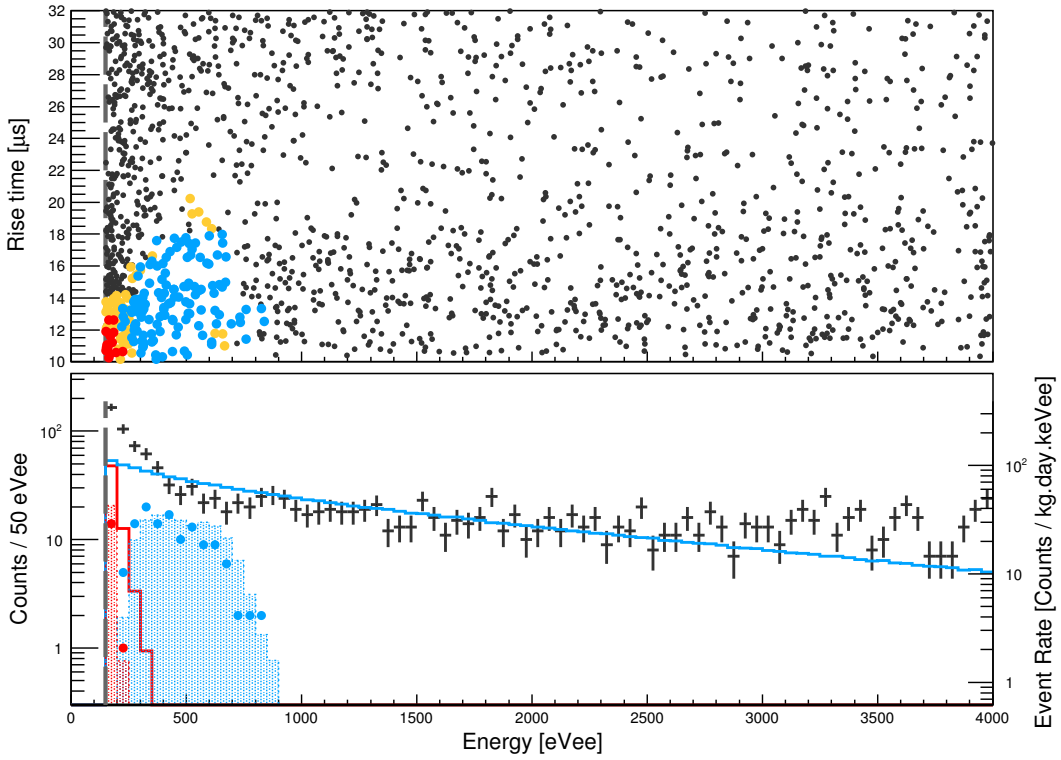

Figure 5. Top panel: distribution of the 1620 events recorded during the physics run in the preliminary ROI. Events that fail the BDT cut for any of the WIMP masses are shown in black dots. Events accepted as candidates for 0.5 GeV/c^2 and 16 GeV/c^2 WIMP masses are shown in red and blue, respectively, while for intermediate WIMP masses, candidates are shown in yellow. Bottom panel: the energy spectrum of events recorded during the physics run in the preliminary ROI is indicated by the black markers. Energy spectra of 0.5 GeV/c^2 and 16 GeV/c^2 WIMP candidates are shown in red and blue dots. The energy spectra before and after the BDT cut of simulated 0.5 GeV/c^2 (resp. 16 GeV/c^2) WIMPs of cross section $\sigma_{excl} = 4.4 \times 10^{-37}$ cm^2 (resp. $\sigma_{excl} = 4.4 \times 10^{39}$ cm^2) excluded at 90 % (C.L.) are shown in unshaded and shaded red (resp. blue) histograms, respectively.

matter search run will lead to an improvement of several orders of magnitude in the sensitivity to low mass WIMPs.

5. SPC calibration with a laser

The NEWS-G collaboration has recently reported on a novel precision laser-based calibration that allowed for the the first-ever measurement of the single-electron-response (SER) in SPCs. The details of this technique and results are presented in [29] A monochromatic UV laser beam with a variable intensity is pulsed to extract single photo-electrons from the inner surface of the SPC at a precise time. The SPC data acquisition is triggered using the laser signal in a photo detector (PD). A schematics of the experimental setup is shown in figure 9.

The study of the SER in SPC using the laser calibration system, allows for the precise measurement of electron transport parameters such as drift time, diffusion coefficients, and electron avalanche gain. In combination with an internal ^{37}Ar source calibration, precise

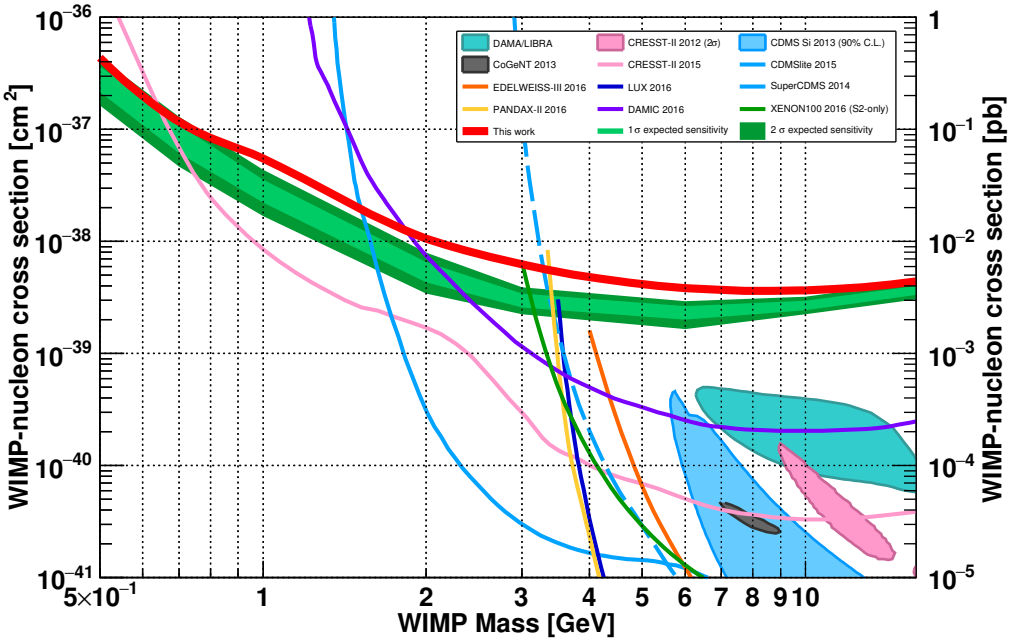

Figure 6. Constraints in the Spin-Independent WIMP-nucleon cross section vs. WIMP mass plane. The result from this analysis is shown in solid red together with the expected 1 σ (resp. 2σ) sensitivity from our background-only model in light green (resp. dark green). Signal hints reported by the CDMS-II Si [16], CoGeNT [17], DAMA/LIBRA [18, 19] and CRESST-II phase 1 [20] experiments are shown in colour contours. Results reported as an upper limit on the WIMP-nucleon cross section are shown in solid and dashed lines for the following experiments: DAMIC [21], LUX [22], XENON100 [23], CRESST-II [24], CDMSlite [25], SuperCDMS [26], EDELWEISS [27] and PANDAX-II [28].

measurements of the gas W-value and Fano factor can be obtained (figure 12). The calibration system can be used during a dark matter search run to monitor the gain and drift velocities over time (figure 13). Additionally, the SPC trigger efficiency can be measured accurately using events triggered by the laser PD (figure 11).

6. Recent developments on the SPC sensors

6.1. NEWS-G detector operation conditions

The spherical proportional counter has been invented and developed by Ioannis Giomataris group in Saclay in collaboration with the Aristotle University of Thessaloniki group. It combines detection threshold in the single electron level along with a large detection volume $\mathcal{O}$ (1 m^3) which in the simplest case can be read-out with a single channel. The detection technique relies also on the alternation of the target gas mixture to include light elements such as neon, helium and hydrogen. For increased sensitivity, the detector is operated at a few bar pressure. Furthermore, to ensure single electron sensitivity, high gain is required. The high pressure and high gain operation relies heavily on the anode and its support structure, the sensor, and demands response homogeneity, charge collection, charge evacuation, and stability. The two key issues that have to be addressed for the NEWS-G detector design to achieve the above goals are: a) the distortion of the radial electric field due to supporting structure, and b) the electric field

Figure 7. Technical drawings of the high purity (C10100 copper) 140-cm SPC to be installed first at LSM, and then at SNOLAB.

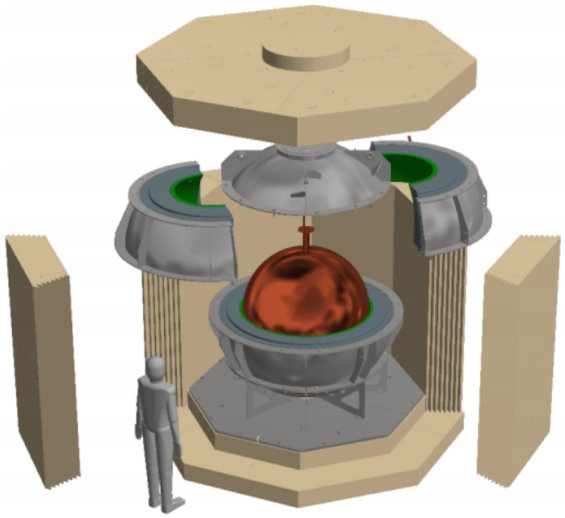

Figure 8. Technical drawings of the NEWS-G experiment at SNOLAB, showing an exploded view of the 140-cm SPC surrounded by a compact lead and polyethylene shielding.

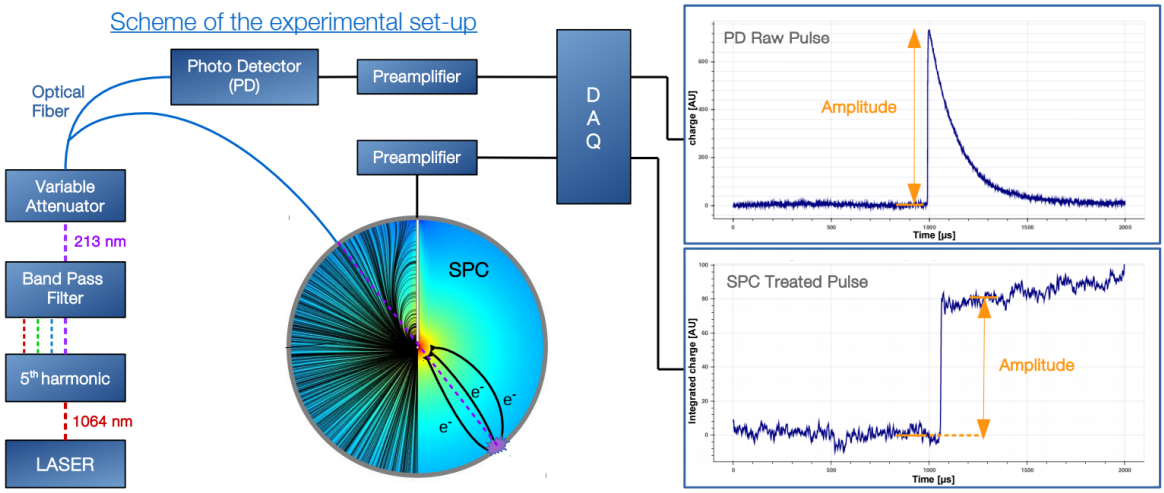

Figure 9. Laser-based calibration: The 213 nm laser light is sent through an optical fiber splitter to both the PD (which triggers the acquisition) and the SPC to extract photo-electrons from the inner surface of the vessel. The two panels on the right show a typical PD signal (raw pulse on top panel) together with the resulting SPC signal (treated pulse on bottom panel) from a single electron reaching the sensor and undergoing an avalanche of average gain. The time delay between the SPC and the PD pulse corresponds to the drift time of the electron from the surface to the sensor.

weakness at the large radii of large volume SPC. Here, we present the two main developments

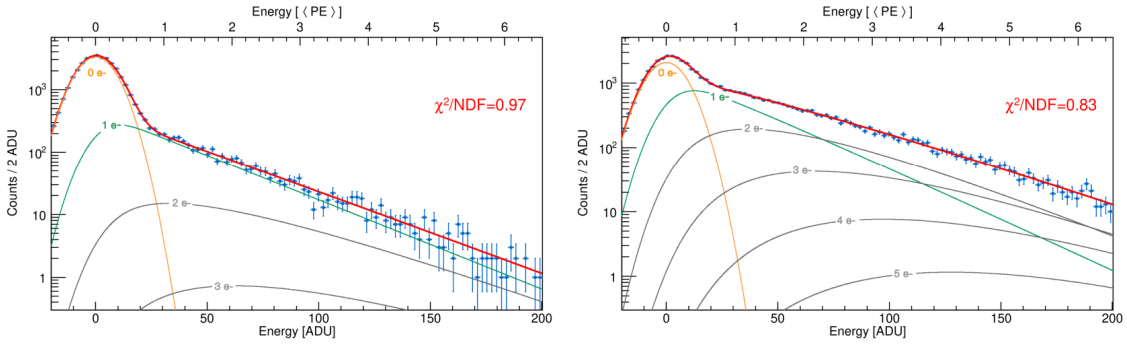

Figure 10. Energy spectra of laser-induced events associated with low (left panel) and high (right panel) PD pulse amplitudes. In both panels, the fit of our model to the data is shown as a solid red line. The relative contribution of the null-events, single and multiple electron events are shown as solid orange, green and gray lines, respectively.

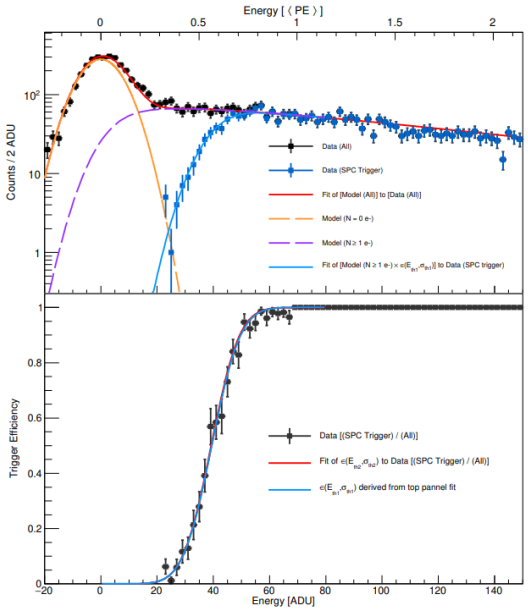

Figure 11. Top Panel: Energy spectrum of laser-induced events with (blue markers) or without (black markers) triggering on the SPC channel. Bottom panel: Relative fraction of events triggering on the SPC channel as a function of the energy. The error bars indicate the statistical (binomial) uncertainty at the corresponding energy.

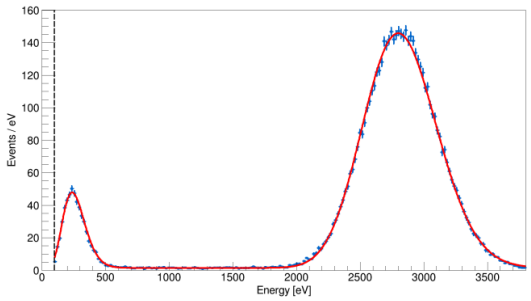

Figure 12. Energy spectrum of non laser-induced events recorded during laser calibration measurements in Ne + CH4 (2%) at 1.5 bar with HV1 = 1150 V. The spectrum clearly shows the 270 eV and 2822 eV lines of X-rays from electron capture in the L- and K-shell of ^{37}Ar, respectively. The energy scale is determined based on the position of the 2822 eV peak. The dashed line indicates the analysis threshold that was set at 100 eV. The solid red line indicates the fit of our model to the data..

in NEWS-G to tackle these issues: the single anode resistive glass correction electrode sensor and the multi-anode sensor (ACHINOS).

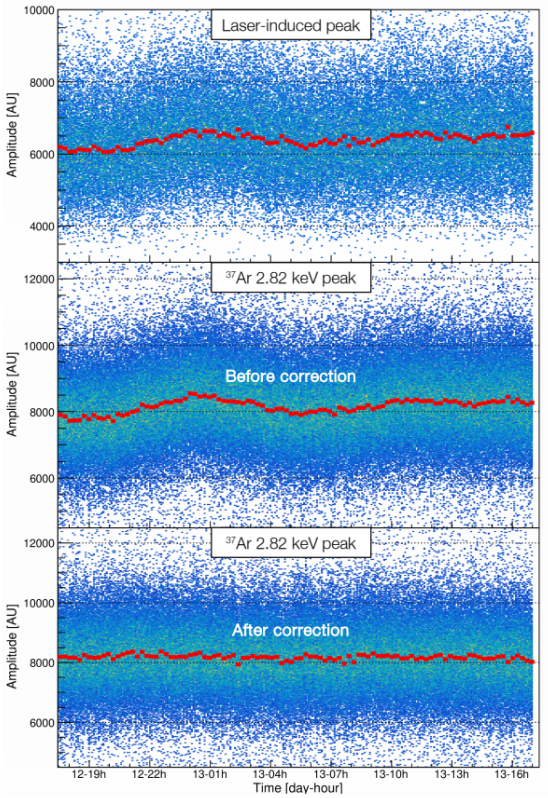

Figure 13. Monitoring of the stability of the gain over time using a UV laser. The top panel shows the distribution in SPC pulse amplitude vs. time of laser-induced events corrected for the laser instability using the PD pulses amplitude. The middle and bottom panels show the distribution of ^{37}Ar 2822 eV events before (middle panel) and after (bottom panel) correcting for gain variations using the position of laser-induced events. The red markers indicate the center of a Gaussian fitted to amplitude spectra for slices in time of 15 min width.

6.2. The single anode resistive glass sensor

The correction electrode is essential for the electric field tuning in realistic detector geometries, affecting the uniformity of response of the detector as a function of the initial ionization position. In its simplest form, the correction electrode is the grounded metallic rod, which shields the gas volume from the electric field of the anode wire. In the absence of the rod, a large fraction of the electric field lines would terminate on the wire, rather than the anode, resulting in the loss of ionization electrons. The beneficial effect of the metallic rod is demonstrated by comparing the electric field configurations in Fig. 14(b) and 14(c), obtained with Finite Element Method (FEM) software, to the ideal case shown in Fig. 14(a). A more homogeneous electric field through the volume of the detector and close to the surface of the anode can be obtained by adding a second correction electrode, complementary to the grounded metallic rod. This electrode is thinner, 1 mm to 2 mm in diameter, and shorter than the rod and it is placed a few millimeters from the anode. An independent electric voltage can be applied to this electrode. The effect of the second correction electrode is shown in Fig. 14(d), providing higher electric field homogeneity and, thus, uniform response for large zenith angles. The electric field around the anode can be fine-tuned by varying the voltage on the surface of the second correction electrode. This is particularly important for the hemisphere containing the grounded rod.

The correction electrode provides a simple but effective solution to the in-homogeneity of the electric field. The correction electrode is positioned a few millimeters from the surface of the anode, supported by the grounded rod. The testing of the first prototypes constructed, displayed in Fig. 15, has demonstrated that due to the anode-electrode proximity it is impractical to implement such a correction electrode using metallic or any conductive materials due to increased sparking rate and intensity.

The alternative is the use of resistive materials as electrodes, which has been shown [30] to

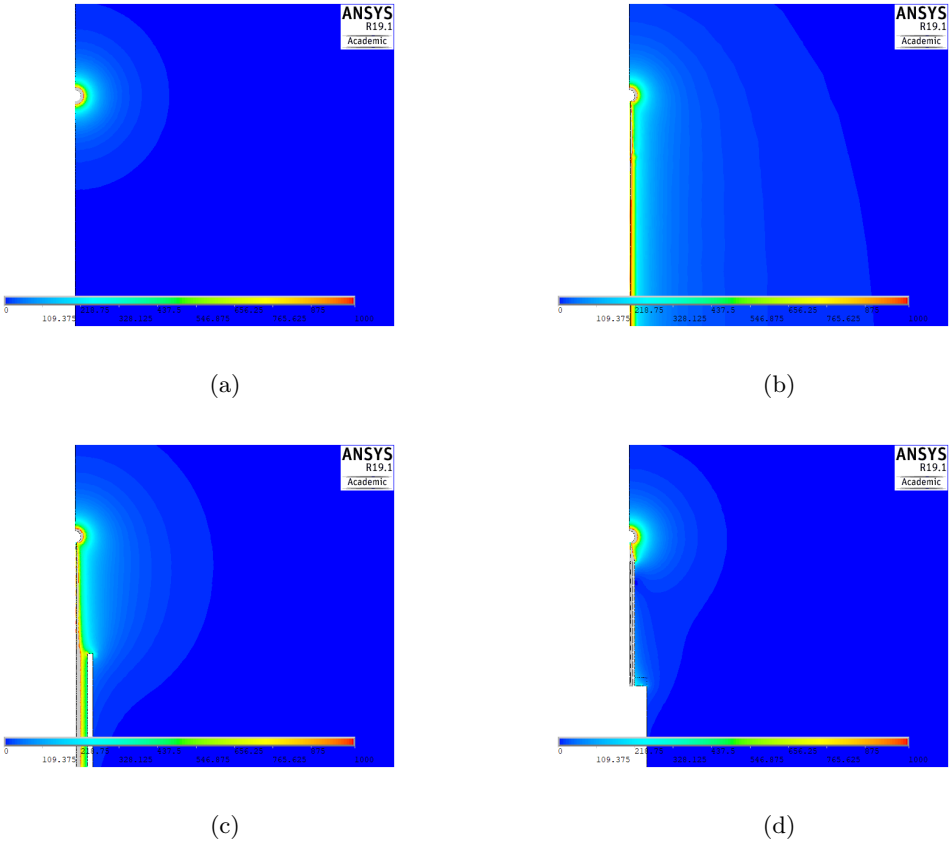

Figure 14. Electric field equipotential lines calculated using FEM software for a 15 cm radius spherical proportional counter with a 1 mm radius anode at 2000 V (a) for the ideal case comprising just the anode at high voltage, (b) including the anode wire to supply the high voltage, (c) including the grounded metallic rod surrounding the anode wire, and (d) including a second glass electrode placed 3 mm from the anode and set to 250 V.

reduce the spark rate and intensity in many detector designs and provide higher gain operation and increased operational stability. The resistivity in these materials, is high enough to quench sparks and allow normal detector operation in the occasion of a spark, while it is adequately low to prevent charging-up. After testing a series of materials with varied resistivities, soda lime glass provided the best results in terms of spark quenching and charge evacuation. The electrodes used were in the form of cylindrical tubes with an 1.85(1.2) mm external(internal) diameter. The volume resistivity of these glass tubes was found to be approximately $\rho = 5.05 \cdot 10^{10}$ $\Omega\cdot$ cm.

6.2.1. Development of the resistive glass electrode prototypes The rod with the glass electrode structure is presented in Fig. 15(a). The internal surface of the glass tube is covered with a layer of conductive glue and electric potential can be applied through a thin wire. This conductive layer facilitates the application of the electric potential on the glass electrode and shields from the influence of the wire's electric field. The external part of the layer is covered with insulating glue to avoid sparks between the conductive layer and the rod. The wire of the anode passes through the glass tube and is aligned by a short insulating tip. In Fig. 15(b), the constructed module is presented. The module is composed of a 2 mm diameter anode made of stainless steel.

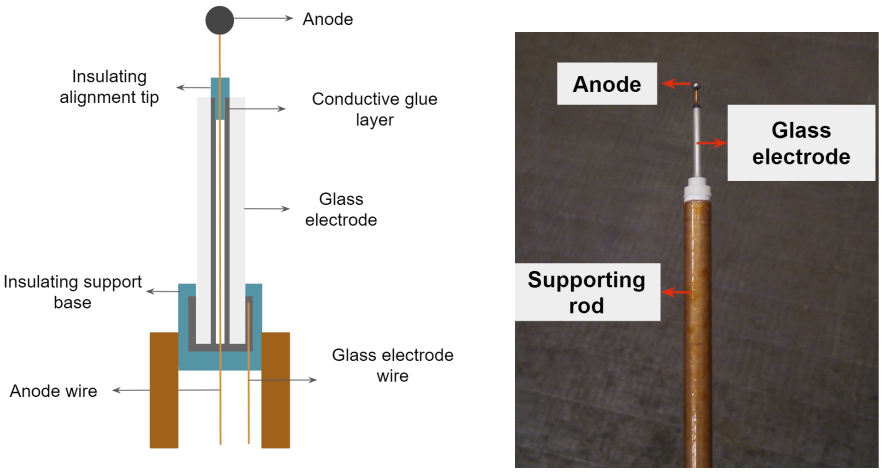

Figure 15. Module with a cylindrical glass correction electrode: (a) schematic and (b) implementation.

The anode is connected to the high voltage power supply with a thin wire. The glass tube has a length of 20 mm and the distance between the ending edge of the tube and the surface of the anode is 3 mm. The module is at the center of a spherical, stainless steel vessel of 15 cm radius and is supported by a copper rod with a 4 mm (6 mm) inner (outer) diameter.

6.2.2. Performance of the resistive glass electrode prototypes The detector operation with resistive glass electrode sensors displayed very satisfying results in terms of homogeneity and stability. In Fig. 16(b) we present the pulse height distributions from the detector irradiation by an ^{55}Fe (5.9 keV X rays) in two zenith angles one at 90° and at 180° to the grounded rod. The detector was filled with 1 bar of He:Ar:CH_4 (92%:5%:3%) with the anode and second correction electrode voltages set at 1450 V and 200 V, respectively. The detector response is similar in the two cases demonstrating that any distortions on the electric field due to the wire are corrected by the use of the resistive electrode. Nonetheless, the main goal was the high pressure operation of the detector with stability even when voltages over 2000 V are applied on the anode. In Fig. 17 the stable operation of the detector in 2 bar of He:Ar:CH_4 (87%:10%:3%) at a voltage of 2350 V applied on the anode and 0 V applied on the correction electrode is shown. The line measured is the 6.4 keV X ray fluorescence of the ^{55}Fe K-line emitted homogeneously from the detector vessel stainless steel walls. The result shows that the detector operated for 12 days without any sparks for the whole duration. A more complete study of the single anode resistive glass sensor can be found at [31].

6.3. The ACHINOS multi-anode sensor

The ACHINOS multi-anode sensor consists of a set of anode balls uniformly distributed around a central sphere at an equal distance from the center of the detector. Insulated wires support the anode balls and apply the high voltage (HV_1) on them. These wires have a constant length and are fixed perpendicularly to the surface of the central sphere in such a way that all the anode balls are on a virtual sphere. The central sphere is made of either highly resistive material or a total insulator covered by a resistive surface, thus making it possible to apply voltage (HV_2) on its surface (bias electrode). The value of HV_2 is chosen to optimize the electric field configuration and improve the energy resolution of the detector. The central electrode is held in the center of

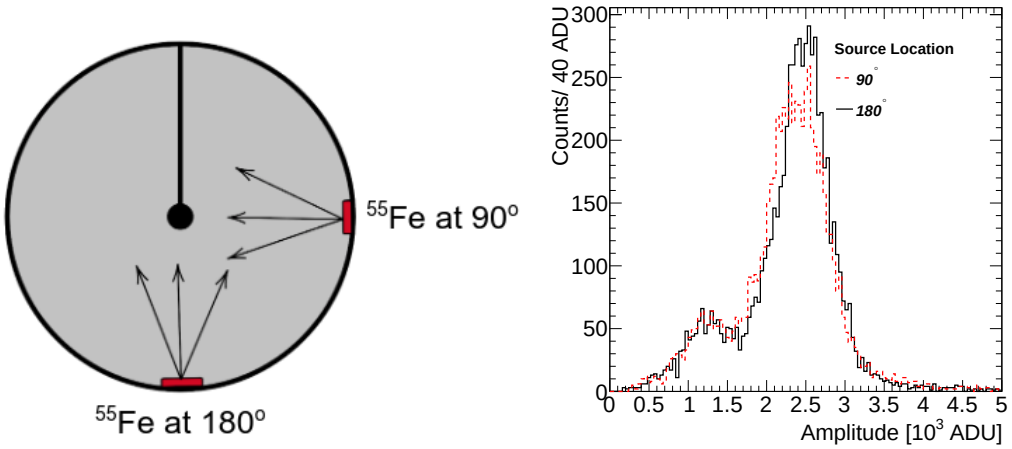

(a) (b)

Figure 16. (a) The source position in the two irradiation zenith angles, (b)The overlaid amplitude distributions for the recorded pulses, for 5.9 keV X rays from an ^{55}Fe source located inside the detector placed at a zenith angle of 90° (red) and 180° (black), relative to the grounded rod.

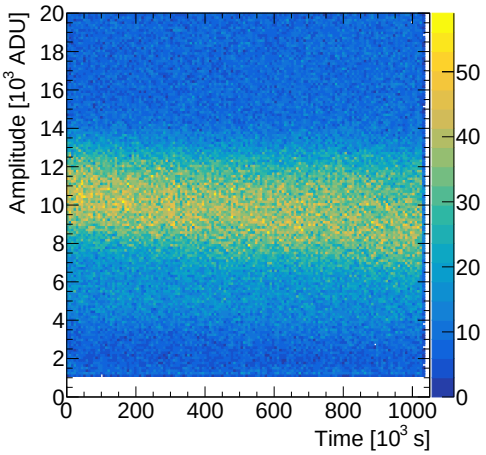

Figure 17. Pulse height as a function of time recorded using a module with a second correction electrode at 0 V, with an anode voltage of 2350 V in a detector filled with 2 bar of He:Ar:CH_4 (87%:10%:3%). The decrease in pulse height over time is due to contaminants, such as oxygen, leaking into the detector. Detector operation is stable and no discharges are observed.

the detector by a hollow metallic rod through which the different wires pass. The example of an 11-anode ACHINOS is displayed in Fig. 18(a). In Fig 18(b) is displayed the streamlines of the electric field induced by the applied high voltage on the anodes of the ACHINOS module. The motivation for the development of such an instrument is to provide an increased electric field in the large radii of large spherical proportional counters (tenths of cm in diameter) which in the case of single anode sensors can be below 0.1 V/cm. Such electric field magnitudes results in increased drift time of electron and ions and makes the operation of the detector sensitive to attachment in the case of contaminants (e.g. O_2, H_2) presence. The detector could be operated with a sensor equipped with anodes of larger diameter (over a few mm) but the small increase

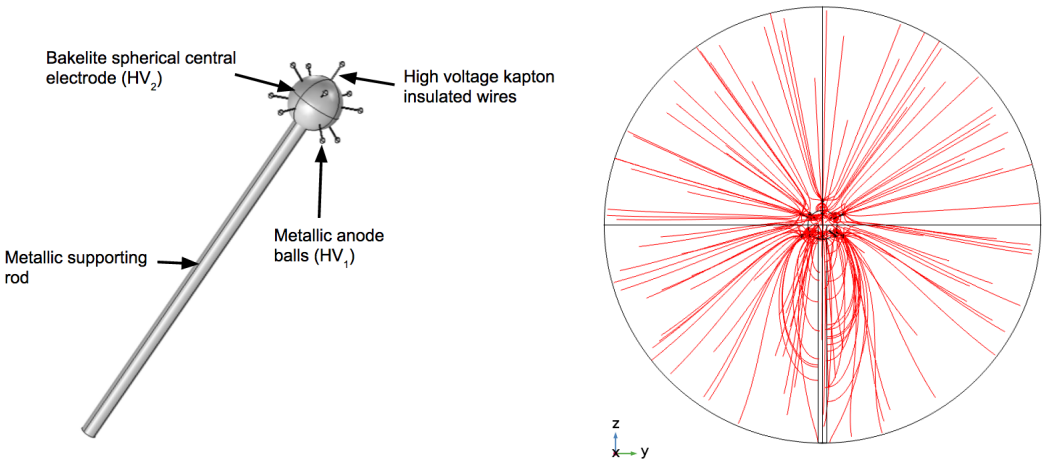

(a) (b)

Figure 18. (a) The design of an ACHINOS module with 11 anodes. The anodes are placed at an equal distance from the center of the spherical central electrode. (b) Streamlines of the electric field in three dimensions for $HV_1 = 2000$ V and $HV_2 = 0$ V (FEM simulation).

on the electric field in large radii, as displayed at Fig. 6 significantly limits the gain capabilities of the detector due the gain dependence on the reduce electric field E/P (where P is the pressure of operation). The ACHINOS sensor provides the capability to maintain high gain operation

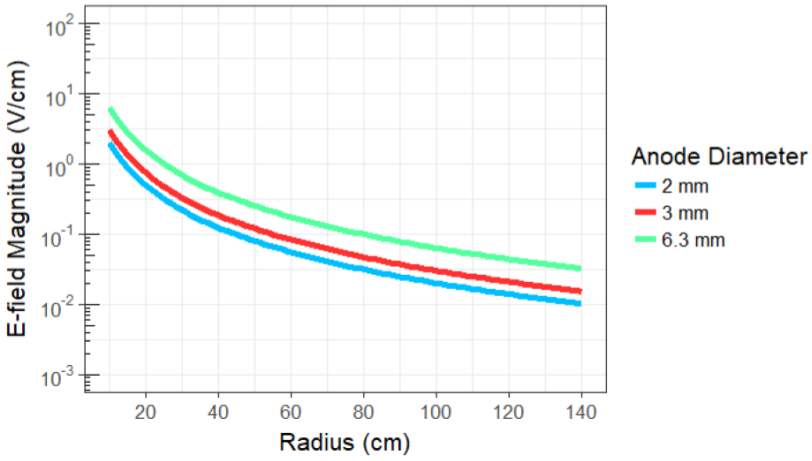

Figure 19. Comparison of the electric field vs radius in a spherical proportional counter with sensors equipped with anodes of 2 mm, 3 mm, and 6.3 mm in diameter.

by using low diameter anodes (below 2 mm) and in the same time increase the strength of the electric field in the detector volume by increasing the number of anodes and their distance from the central secondary electrode. As a result electrons liberated by ionization in the volume of the detector will drift under the influence of the electric field of the eleven balls collectively. Their drift will bring them close to one of the anode balls, where the electric field is increasing strongly and the charge multiplication will take place. The effect of multiple anodes being used in an

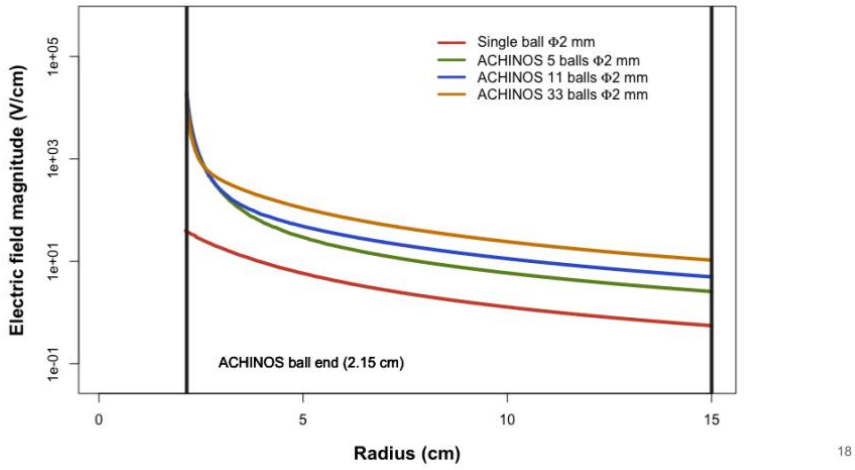

Figure 20. Electric field magnitude versus the radius inside the detector in the case of a) a single 2 mm in diameter anode ball placed in the center of the 300-mm diameter detector, b) the ACHINOS sensor made of five balls, c) the ACHINOS sensor made of eleven balls d) the ACHINOS sensor made of thirty-five balls. In all three cases of the ACHINOS sensor, the balls are distributed on a 41 mm diameter sphere placed in the center of the detector.

ACHINOS sensor versus a single anode sensor is displayed in figure Fig. 20. The plot displays the magnitude of the electric field starting from the surface of the anode placed parallel to the Z-axis ("north") of an ACHINOS sensor and compares it with the electric field of a single ball sensor with its anode in the center of the detector, placed on the surface of a central electrode of the same radius as in an ACHINOS sensor. In both cases an electric potential of 2000 V is applied. The electric field close to the surface of the shell of the detector is higher in the case of an ACHINOS sensor (approximately 9 times higher for an 11-ball ACHINOS) than in the case of the single ball sensor.

6.3.1. Developments and performance of the ACHINOS prototypes The first ACHINOS prototypes (Fig. 22(a)) were made using metallic anodes (1-2 mm in diameter) fixed at 7 mm from the spherical central electrode surface which was made of bakelite. The diameter of the bakelite ball varied between 25-30 mm. These modules were tested using an ^{55}Fe which was placed inside the spherical vessel of the detector. The rise time distributions of the pulses measured using an 11-anode ACHINOS module and a single ball sensor of the same anode diameter are compared in Fig. 22. Since the rise time of the pulses is directly related to the longitudinal diffusion of the primary electrons and the electric field magnitude, the rise time dispersion is an indicator of the reduction in the drift time dispersion of the primary electrons. The principle of the ACHINOS design is clearly displayed by the difference in the upper limits of the rise time distribution of the two sensors, were in the case of the ACHINOS sensor the maximum rise time is $\sim$8.7 times less than the maximum rise time of the single anode sensor for the same operating conditions.

Although the first ACHINOS prototypes proved that these modules can become a valuable tool to make the SPC a more scalable detector, due to the fact that the anodes had to be place in their position manually, proved to be a limiting factor in terms of energy resolution. Small differences in anode placement had as a consequence some anodes having different gain from

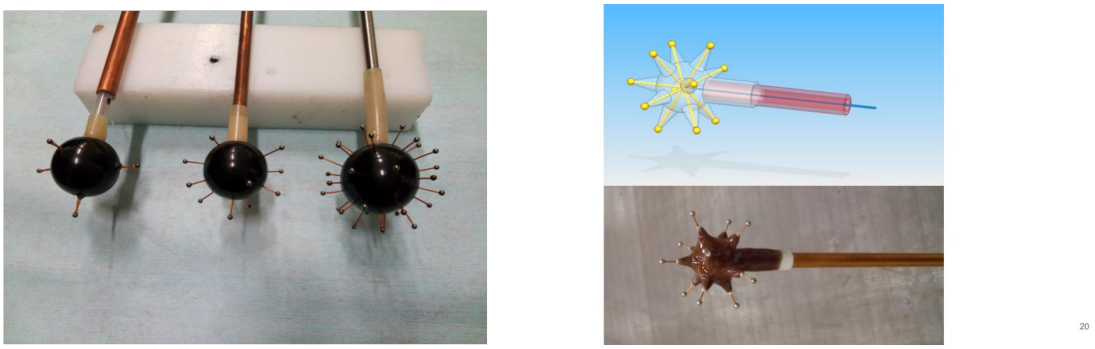

(a) (b)

Figure 21. (a) The first generation of ACHINOS prototypes. In particular the modules have 5, 11, and 33 anodes of 2 mm in diameter and the central secondary electrode is composed of Bakelite. (b) The second generation of ACHINOS prototypes. In this design, the central electrode which acts also as a support structure is made of PLO and is constructed using 3D printing. The insulating PLO is covered with a resistive paste, in this case copper plus Araldite, so the voltage can be applied on the secondary electrode.

the others and secondary peaks appearing for the same measured X-ray line, more details can be found at [32]. For that reason the second generation of ACHINOS sensor is based on the

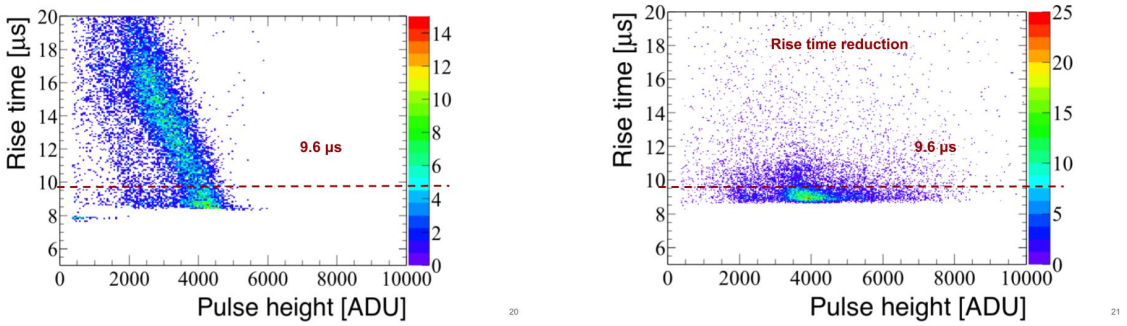

(a) (b)

Figure 22. The pulse height versus the rise time measured by a SPC filled with a He:Ar:CH_4 (80:11:9) gas mixture at 640 mbar in (a) the case of a single anode sensor equipped with a 2-mm anode ball, with a high voltage of 2015 V applied on the anode (HV_1) (b) the case of an 11-ball ACHINOS sensor with 2-mm anode balls, with a high voltage of 2015 V applied on the anodes (HV_1) and of -200 V applied on the central electrode (HV_2). The rise time distribution of the single ball sensor has a full width of 9.6 µs whereas the one of ACHINOS has a full width of 1.1 µs.

3D printing technology for the construction of the central electrode which acts as a support structure for the anodes. Beyond the manufacturing ease of the sensors this technique allows for a very accurate placement of the anodes limiting the effect of different gain for some of them. To allow the voltage application on the surface of the secondary electrode, the insulating material is covered by a resistive paste which is connected to a high voltage wire. The mixture of the paste is currently under study. By now the combination of copper and graphite with Araldite has provided the most promising results. The design and an implementation of a second generation

ACHINOS sensor is presented in Fig. 22(b). In Fig. 23 the 5.9 keV X ray line of an ^{55}Fe source measured with an ACHINOS of the second generation is presented. The results is satisfying in terms of homogeneity as all the anodes appear to have similar gain. The limiting factor in the second generation modules is sparks that appear in detector operation over a few hundred mbar. The main factor that causes this limitation is the preparation procedure for these mixtures which is not yet optimized in terms of mixture homogeneity, percentage of conductive material (copper dust or graphite dust for example) and creation of air pockets (bubbles). These factors are under intense study and are expected to be optimized soon.

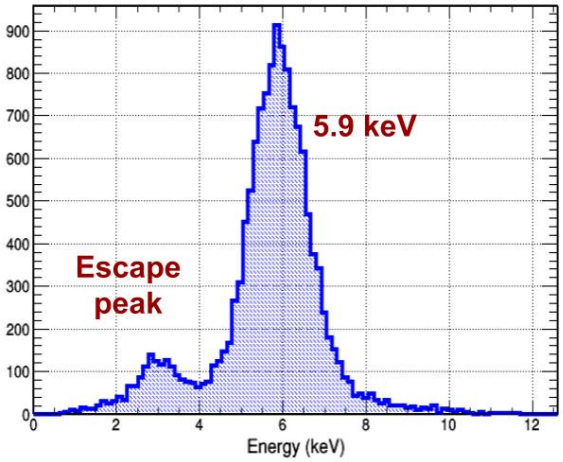

Figure 23. Pulse height distribution, of the signal produced by the 5.9 keV X ray line of an ^{55}Fe source. The SPC was filled with a He:Ar:CH_4 (56:37:7) gas mixture at 455 mbar. The high voltage applied on the 2 mm in diameter anodes (HV_1) of the 11-ball ACHINOS was 1100 V and on the central electrode (HV_2) was −100 V.

7. Conclusion and outlook

The NEWS-G SPC filled with low atomic mass target is an especially well suited detector to the search for light WIMPs. Recent results from the operation of SEDINE at LSM provide competitive constraints on the WIMP-nucleon cross section below 1 GeV/c^2. The future operation of the 140-cm ultra-low background at SNOLAB, with novel sensor technology and detector monitoring with a laser will allow the exploration of order of magnitudes of new WIMP parameter space and could shed light on the nature of dark matter.

Acknowledgments

We would like to acknowledge the technical support provided by the Laboratoire Souterrain de Modane. The operation of SEDINE has been partially funded by the European Commission astroparticle program ILIAS (Contract R113-CT-2004-506222). This work was undertaken, in part thanks to the funding from the Canada Research Chairs program, as well as from the French National Research Agency (ANR-15-CE31-0008).

References

[1] G. Bertone, Particle Dark Matter: Observations, Models and Searches, 2010, Cambridge University Press.
[2] D. Clowe, et al., A Direct Empirical Proof of the Existence of Dark Matter, 2006, *Astrophys. J.* **648**, L109.
[3] P.A.R. Ade, et al., Planck 2015 results - XIII. Cosmological parameters, 2016, *Astron. Astrophys.*, A13.

[4] J.L. Feng, Dark Matter Candidates from Particle Physics and Methods of Detection, 2010, *Annu. Rev. Astron. Astrophys.* **495 - 545**,
[5] G. Jungman, M. Kamionkowski and K. Griest, Supersymmetric dark matter, 1996, *Phys. Rep.* **267**, 195 - 373.
[6] O. Buchmueller, et al., 2012, *Eur. Phys. J.* C **72**, 2243.
[7] R. Essig, et al., Working Group Report: New Light Weakly Coupled Particles, 2013, arXiv:1311.0029 [hep-ph].
[8] D. Profumo, Good NEWS for GeV Dark Matter Searches, 2015, arXiv:1507.07531 [hep-ph].
[9] K. Petraki and R.R. Volkas, Review of asymmetric dark matter, 2013, *Int. J. Mod. Phys. A* **28**, 1330028.
[10] K. Zurek, 2014, *Phys. Rep.* **537**, 91 - 121.
[11] K. Schneck, et al., Dark matter effective field theory scattering in direct detection experiments, 2015, *Phys. Rev. D* **91**, 092004.
[12] I. Giomataris, et al., A novel large-volume spherical detector with proportional amplification read-out, 2008, *J. Instrum.* **3, P09007**.
[13] G. Gerbier, et al., NEWS : a new spherical gas detector for very low mass WIMP detection, 2004, arXiv:1401.7902 [astro-ph.IM].
[14] M. Laubenstein, et al., Underground measurements of radioactivity, 2004, *Appl. Radiat. Isot.* **61**, 167 - 172.
[15] Q. Arnaud, et al., First results from the NEWS-G direct dark matter search experiment at the LSM, 2018 *Astropart. Phys.* **97** 54-62.
[16] R. Agnese, et al., Silicon Detector Dark Matter Results from the Final Exposure of CDMS II, 2013, *Phys. Rev. Lett.* **111**, 251301.
[17] C.E. Aalseth, et al., CoGeNT: A search for low-mass dark matter using *p*-type point contact germanium detectors, 2013, *Phys. Rev. D* **88**, 012002.
[18] R. Bernabe, et al., First results from DAMA/LIBRA and the combined results with DAMA/NaI, 2008, *Eur. Phys. J.* C **56**, 333-355.
[19] C. Savage, et al., Compatibility of DAMA/LIBRA dark matter detection with other searches, 2009, *J. Cosmol. Astropart. Phys.*, 010.
[20] G. Angloher, et al., Results from 730 kg days of the CRESST-II Dark Matter search, 2012, *Eur. Phys. J. C* **72**, 1971.
[21] A. Aguilar-Arevalo, et al., Search for low-mass WIMPs in a 0.6 kg day exposure of the DAMIC experiment at SNOLAB, 2016, *Phys. Rev.* D **94**, 082006.
[22] D.S. Akerib, et al., Improved Limits on Scattering of Weakly Interacting Massive Particles from Reanalysis of 2013 LUX Data, 2016, *Phys. Rev. Lett.* **116** 161301.
[23] E. Aprile, et al., Low-mass dark matter search using ionization signals in XENON100, 2016, *Phys. Rev.* D **94**, 092001.
[24] G. Angloher, et al., Results on light dark matter particles with a low-threshold CRESST-II detector, *Eur. Phys. J.* C **76**, 25.
[25] R. Agnese, et al., New Results from the Search for Low-Mass Weakly Interacting Massive Particles with the CDMS Low Ionization Threshold Experiment, 2016, *Phys. Rev. Lett.* **116**, 071301.
[26] R. Agnese, et al. Search for Low-Mass Weakly Interacting Massive Particles with SuperCDMS, 2014, *Phys. Rev. Lett.* **112**, 241302.
[27] E. Armengaud, et al., Final results of the EDELWEISS-II WIMP search using a 4-kg array of cryogenic germanium detectors with interleaved electrodes, 2011, *Phys. Lett.* B **702**, 329 - 335.
[28] A. Tan, et al., Dark Matter Results from First 98.7 Days of Data from the PandaX-II Experiment, 2016, *Phys. Rev. Lett.* **117**, 121303.
[29] Q. Arnaud, et al., Precision laser-based measurements of the single electron response of SPCs for the NEWS-G light dark matter search experiment, 2019, arXiv:1902.08960 [physics.ins-det].
[30] T. Alexopoulos, A spark-resistant bulk-micromegas chamber for high-rate applications, *Nucl. Instrum. Methods Phys. Res. A* **640**, 110-118.
[31] I. Katsioulas, et al., A sparkless resistive glass correction electrode for the spherical proportional counter, 2018, *J. Instrum.* **13**, P11006.
[32] A. Giganon, et al., A multiball read-out for the spherical proportional counter, 2017, *J. Instrum.* **12**, P12031.